Snowflake Size Spectra Retrieved from a UHF Vertical Profiler

ANDREW J. NEWMAN* AND PAUL A. KUCERA+

Department of Atmospheric Sciences, University of North Dakota, Grand Forks, North Dakota

CHRISTOPHER R. WILLIAMS

Cooperative Institute for Research in Environmental Sciences, University of Colorado, Boulder, Colorado

LARRY F. BLIVEN

Instrumentation Sciences Branch, NASA Goddard Space Flight Center, Greenbelt, Maryland

(Manuscript received 4 January 2008, in final form 11 August 2008)

ABSTRACT

This paper develops a technique for retrieving snowflake size distributions (SSDs) from a vertically pointing 915-MHz vertical profiler. Drop size distributions (DSDs) have been retrieved from 915-MHz profilers for several years using least squares minimization to determine the best-fit DSD to the observed Doppler spectra. This same premise is used to attempt the retrieval of SSDs. A nonlinear search, the Levenberg–Marquardt (LM) method, is used to search the physically realistic solution space and arrive at a best-fit SSD from the Doppler spectra of the profiler. The best fit is assumed to be the minimum of the squared difference of the log of the observed and modeled spectrum power over the precipitation portion of the spectrum. A snowflake video imager (SVI) disdrometer was collocated with the profiler and provided surface estimates of the SSDs. The SVI also provided estimates of crystal type, which is critical in attempting to estimate the density–size relationship. A method to vary the density–size relationship during the event was developed as well. This was necessary to correctly scale the SVI SSDs for comparison to the profiler-estimated distributions. Five events were examined for this study, and good overall agreement was found between the profiler and SVI for the lowest profiler gate (225 m AGL). Vertical profiles of SSDs were also produced and appear to be physically reasonable. Uncertainty estimates using simulated Doppler spectra show that the retrieval uncertainties are larger than that for rainfall and can approach and exceed 100% for situations with large spectral broadening as a result of atmospheric turbulence. The larger uncertainties are attributed to the lack of unique Doppler spectra for quite different SSDs, resulting in a less well-behaved solution space than that of rainfall retrievals.

1. Introduction

Vertically pointing Doppler radars have been used to retrieve drop size distributions (DSDs) since the early 1960s (Rogers and Pilié 1962; Caton 1966; Battan and Theiss 1966). The basic premise of this idea is that given a unique fall speed–size relationship for the hydrometeors being observed, the Doppler spectra can be related back to diameter and number concentration. These early attempts at DSD retrievals had large uncertainties as a result of their analysis techniques. Atlas et al. (1973) showed that a vertical air motion accuracy of ± 1 m s^{-1} was all that should be expected from these early attempts, which resulted in an uncertainty of one order of magnitude in the estimated DSDs. This is because ambient air motions shift the precipitation Doppler spectra (i.e., an updraft (downdraft) of 1 m s^{-1} will decrease (increase) the fall speed of all hydrometeors by 1 m s^{-1}). This shift causes the retrieved DSD to underestimate (overestimate) the concentration of large drops (small drops).

Hauser and Amayenc (1981, 1983) began to lay the groundwork for improved single-frequency (UHF) DSD

* Current affiliation: Department of Atmospheric Science, Colorado State University, Fort Collins, Colorado.

+ Current affiliation: National Center for Atmospheric Research, Boulder, Colorado.

Corresponding author address: Andrew J. Newman, Department of Atmospheric Science, Colorado State University, 1371 Campus Delivery, Fort Collins, CO 80523-1371.
E-mail: anewman@atmos.colostate.edu

DOI: 10.1175/2008JTECHA1105.1

© 2009 American Meteorological Society

estimation without the clear-air spectra being observed with the development and testing of the three-parameter (3P) method. This method to retrieve DSDs assumed an exponential size distribution and solves for w (mean air motion), N_0 (intercept parameter) and Λ (slope parameter) simultaneously while ignoring turbulence. The best-fit (w, N_0, and Λ) values to the observed spectrum are determined through a least squares fitting technique. Sangren et al. (1984) suggested that the 3P method could be improved by including turbulence. Williams (2002) developed a technique that estimates both turbulence and mean vertical motion when determining DSDs without knowledge of the ambient air motions. This work uses this basic methodology described in Williams (2002) and applies it to produce retrievals of snowfall size distributions (SSDs) in the precipitating layer, below 3 km above ground level (AGL), of northern plains snowfall events.

An extensive literature search revealed only one prior study using a vertical profiler to retrieve SSDs (Rajopadhyaya et al. 1994). This study examined SSD retrievals above the melting layer in mesoscale convective systems. No prior work using UHF profilers to retrieve SSDs in the precipitating layer have been found by the authors. Therefore, it is of interest to examine the ability of vertical profilers to retrieve microphysical information from snowfall events. In practical terms, our ability to measure snowfall severely lags behind that of rainfall. To more fully understand the global water cycle, improved snowfall estimates need to be made. This work attempts to develop another measurement platform to observe snowfall measurements directly and potentially provide ground validation (GV) for satellite snowfall algorithms.

The paper is organized as follows. The next section provides a general description of the Doppler spectra. Section 3 gives a basic description of the video disdrometer [snowflake video imager (SVI); refer to related paper by Newman et al. (2009)]. SSDs used for the validation of the retrieved SSD are given. Following the data descriptions, the methodology of the retrieval process, uncertainty analysis, and validation of the retrievals are described. In section 4, the results of this study are presented along with a discussion of them. Finally, some concluding remarks and ideas for future work are given.

2. Data description

a. Instrument overview

The 915-MHz profiler and the SVI were collocated at the Glacial Ridge Atmospheric Observatory (GRAO), operated by the University of North Dakota, for all the observations in this study. For reference, the GRAO is located on the Glacial Ridge Nature Conservatory, approximately 25 km east-southeast of Crookston, Minnesota. The profiler-provided vertical profiles of the full Doppler spectra approximately every three minutes at a vertical resolution of 90 m with a range of 225–4500 m above ground level for this study. The raw spectra are corrected for various hardware and filtering effects using National Oceanic and Atmospheric Administration (NOAA) software (P. E. Johnston 2005, unpublished manuscript). The corrected Doppler spectra are used in the profiler retrieval process described in section 3. This software also produces reflectivity (Z), mean Doppler velocity (V) and spectrum width (W) estimates. Besides precipitation information, vertical profiles of the two-dimensional wind field can be made available if desired. Figure 1 gives an example of Z, V, and W values throughout an example snowfall event.

The SVI uses a grayscale charged-coupled device (CCD) grayscale camera with an operational frame rate of 55–58 frames per second (fps). The camera has a pixel resolution of 640 × 240, with an actual resolution of 0.05 mm in the horizontal and 0.1 mm in the vertical. This corresponds to an image size of 32 × 24 mm in the focal plane. The image data is processed using National Instruments' LabVIEW software. Text output describing every particle imaged is produced, and the SSDs are produced from these files. The SVI may have sampling advantages over other disdrometers in snowfall because it has minimal instrument-caused interference with its sample volume and does not require any type of shielding for operation. Refer to Newman et al. (2009) for more information about the SVI.

b. Doppler spectra

Because UHF profilers observe both Bragg and Rayleigh scattering (Gossard and Strauch 1983; Gage et al. 1999), the observed Doppler velocity spectra can be written as (following Wakasugi et al. 1986, 1987; Williams 2002)

$$S_{\mathrm{obs}}(v) = P_{\mathrm{air}} S_{\mathrm{air}}(v - \bar{w}) + S_{\mathrm{air}}(v - \bar{w}) {}^{*} S_{\mathrm{hyd}}(v) + \mathrm{Noise}, \tag{1}$$

where the right-hand side terms are the Bragg (first term) and Rayleigh (second term) scattering components along with the random background noise (third term). The term P_{air} is the magnitude of the Bragg scattering component, which depends on the refractive index gradients in the radar volume; $\bar{w}$ represents the mean vertical velocity in the radar sample volume; v

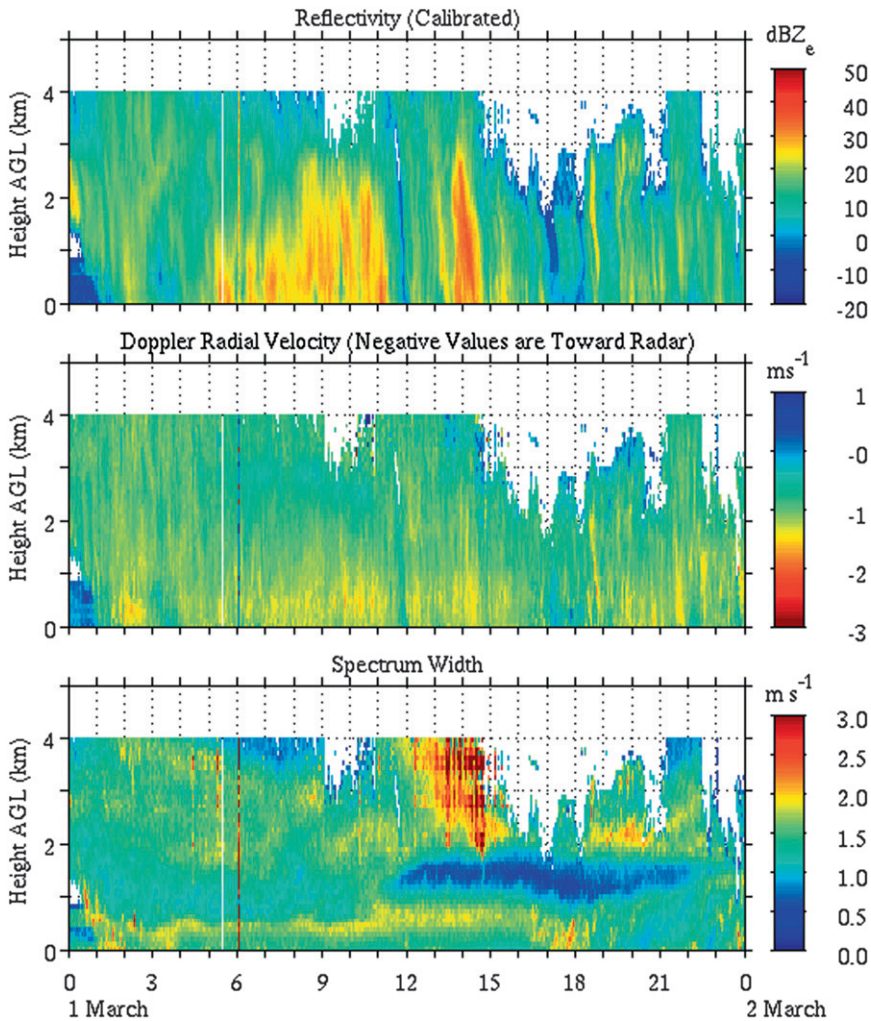

FIG. 1. GRAO profiler calibrated (top) reflectivity, (middle) mean Doppler velocity, and (bottom) spectrum variance for 01 Mar 2007.

represents the Doppler velocity at each spectral point; and * represents the convolution operator. Bragg scattering has been represented as a Gaussian-shaped distribution of turbulent velocities centered on the mean vertical velocity (Currier et al. 1992; Rogers et al. 1993; Gossard 1994; Rajopadhyaya et al. 1993, and others). This Gaussian-shaped distribution is given by

$$S_{\mathrm{Bragg}}(v) = P_{\mathrm{air}} S_{\mathrm{air}}(v - \bar{w}) = \frac{P_{\mathrm{air}}}{\sqrt{2\pi}\sigma_{\mathrm{air}}} \exp\left[\frac{-(v - \bar{w})}{2\sigma_{\mathrm{air}}^2}\right], \tag{2}$$

where σ_{air}^2 is the variance of the distribution, or the variance of the spectral broadening.

Gossard (1988) showed that the second term of Eq. (1), the Rayleigh scattering component, comes from the convolution of the normalized turbulence distribution function shown in Eq. (2) with the hydrometeor spectral density. This can be expressed as (Rajopadhyaya et al. 1998, 1999)

$$\begin{aligned} S_{\mathrm{Rayleigh}} &= S_{\mathrm{air}}(v - \bar{w}) {}^{*} S_{\mathrm{hyd}}(v) \\ &= \frac{1}{\sqrt{2\pi}\sigma_{\mathrm{air}}} \exp\left[\frac{-(v - \bar{w})}{2\sigma_{\mathrm{air}}^2}\right] {}^{*} S_{\mathrm{hyd}}(v), \end{aligned} \tag{3}$$

where the hydrometeor spectral density is given as

$$S_{\mathrm{hyd}}(v) = N(D) D^6 \frac{dD}{dv}. \tag{4}$$

Here, $N(D)$ is the number concentration of the hydrometeor distribution at diameter D, and dD/dv is the coordinate transformation from terminal velocity to diameter space. The D^6 in (4) comes from the Rayleigh

scattering from spherical raindrops. Backscattered energy from irregular-shaped ice crystals and aggregates will be addressed in section 2b. This study uses the exponential distribution to describe $N(D)$. An exponential distribution is given as

$$N(D) = N_0 \times \exp[-\Lambda D], \tag{5}$$

where N_0 is the scale parameter, and Λ is the slope parameter. This distribution has been used to represent the melted diameter distributions of snowfall (Gunn and Marshall 1958; Sekhon and Srivastava 1970). Exponential distributions were also used as a result of their simplicity. Because of the many areas of uncertainty regarding snowfall, a simple initial model seems appropriate. Expansion into more complex distributions can be undertaken in the future.

c. *Video snowflake imager snow size distribution description*

In general, to determine a hydrometeor size distribution from a disdrometer, the number of hydrometeors, sample volume, and bin size need to be known. This can be written as

$$N(D) = \frac{\#\text{Hydrometeors}}{V\Delta D}, \tag{6}$$

where V is the sample volume, and ΔD is the bin interval in millimeters. Equation (6) gives the typical number concentration units of the number per cubic meter per millimeter (# m^{-3} mm^{-1}). The sample volume is determined through various methods depending on the instrument. In the case of the video snowflake imager (SVI), the sample volume is determined by applying the depth-of-field (DOF) relationship explained in Newman et al. (2009) along with the vertical and horizontal extent of the image plane to determine a volume per frame for a given hydrometeor size. The size of the image plane is corrected for border rejection using the method described in Barthazay et al. (2004). This entails subtracting half the length of the imaged particle around the edges of the image to determine the effective cross section of the sample volume. By counting the number of frames processed during a time interval, the total sample volume can be calculated. For the SVI, the number concentration for a specific bin can be written as

$$N(L_{\text{med}}) = \frac{n_{\text{bin}}}{\text{DOF}(L_{\text{med}})W(L_{\text{med}})H(L_{\text{med}})\text{Fr}(2\Delta L)}, \tag{7}$$

where n_{bin} is the number of hydrometeors in the bin defined by the bounds from $(L - \Delta L)$ to $(L + \Delta L)$, $\text{DOF}(L_{\text{med}})$ is the depth of field, $W(L_{\text{med}})$ is the corrected width, $H(L_{\text{med}})$ is the corrected height, and Fr is the number of frames. The number of frames is the number of times the camera images the sample volume for a given integration time. If an SSD was produced using a 1-min integration time and the frame rate was 55 fps, Fr would be the unitless number 3300. Here, L_{med} is used to specify the midpoint of the bin defined by the bounds given above, where L signifies the use of maximum length rather than diameter. Calculating $N(L_{\text{med}})$ at every bin midpoint gives the complete observed size distribution. From the complete distribution, various moments of the distribution can be calculated (i.e., reflectivity factor). Note that when comparing SSD distributions/moments from the SVI to those of the profiler, care must be taken to ensure the correct comparisons are being made because the SVI measures a maximum snowflake length, while the profiler will measure an equivalent ice sphere diameter.

3. Methodology

a. *Profiler retrieval process*

The SSD is estimated by fitting a modeled Doppler spectrum to the observed spectrum. From (3) and (4), there are four parameters in the model Doppler spectrum: parameters $\bar{w}$ and σ^2_{air} describe the air motion shift and spectral broadening, and N_0 and Λ describe the SSD. Minimizing the difference between this four-parameter model and the observed spectrum appears to be an ill-posed problem with many different possible solutions. The number of possible solutions can be reduced by applying the conservation of reflectivity and the conservation of mean Doppler velocity between the model and observed spectra (Williams 2002). That is, the modeled spectrum must have the same total reflectivity and mean Doppler velocity as the observed spectrum. The total reflectivity (in linear units, mm^6 m^{-3}) is defined as (Williams 2002)

$$z = \int_{v_{\min}}^{v_{\max}} S_{\text{obs}}(v)dv = \int_{D_{\min}}^{D_{\max}} N_0 D^6 \exp(-\Lambda D)dD, \tag{8}$$

where $v_{\min}$ and $v_{\max}$ are the limits of integration in the velocity domain, and $D_{\min}$ and $D_{\max}$ are the estimated limits of integration in the diameter domain. The mean Doppler velocity is defined as

$$\begin{aligned} V_{\text{Doppler}} &= \frac{\int_{v_{\min}}^{v_{\max}} vS_{\text{obs}}(v)dv}{\int_{v_{\min}}^{v_{\max}} S_{\text{obs}}(v)dv} = V_{\text{fallspeed}} - \bar{w}, \\ &= \frac{\int_{D_{\min}}^{D_{\max}} v_{\text{fallspeed}}(D)D^6 \exp(-\Lambda D)dD}{\int_{D_{\min}}^{D_{\max}} D^6 \exp(-\Lambda D)dD} - \bar{w}, \end{aligned} \tag{9}$$

where $v_{\text{fallspeed}}(D)$ is the terminal velocity–size relationship. Note, positive values of $\bar{w}$ denote upward motion in (9).

As discussed earlier, the mean air velocity causes a shift in the fall speeds and observed Doppler spectrum with upward (downward) motion shifting the fall speeds and observed spectrum toward more upward (more downward) velocities. Because an exponential distribution is used, the mean Doppler velocity constraint cannot be implemented in the same fashion as Williams (2002). Instead, the mean Doppler velocity information will be used to help assess the quality of the model distribution in a different way. The exponential distribution was used in this case because of the complexities of snowfall and the ill-posed solution space noted above. Initial runs were performed with the gamma distribution used in Williams (2002), but the LM method was very unstable, and the extra parameter did not seem to improve the quality of the solution. This may relate to the solution space issues discussed in the appendix.

The validity of using an exponential distribution for estimating the observed SSD may be in question in some cases. Therefore, the gamma distribution was fit to all observed SSDs. The shape parameter μ in the gamma distribution gives the deviation from exponential ($\mu = 0$ for exponential). For the events examined in this study, 84% of the SSDs had a fitted μ within ± 2 of zero. In Brandes et al. (2007), approximately 56% of their observed SSDs had a fitted μ within ± 2 of zero. Speculation as to the causes of these differences is premature, and future work will be done comparing SVI observations to other disdrometers. Comparisons to Particle Size and Velocity (PARSIVEL) data during the Canadian CloudSat/Cloud–Aerosol Lidar and Infrared Pathfinder Satellite Observation (CALIPSO) Validation Project (C3VP) are being prepared for a forthcoming manuscript headed by Dr. Larry Bliven. Overall, no fitted μ values exceeded 0 ± 5 for this study. It was also noted that as the snowfall rate increased, μ trended toward negative values. In fact, μ was almost always negative in heavy snowfall. This tendency was also shown by Brandes et al. (2007, their Fig. 10d).

Two modifications to the terminal fall speed relationships were performed as well. First, most terminal velocity–size relationships for snowfall are developed for either individual crystals or aggregate flakes. Assuming there are situations in which individual crystals are large enough to make a significant contribution to the precipitation return, a combination fall speed–size relationship will have to be used. To achieve this, an appropriate aggregate mass relationship and crystal mass relationship were blended together in the 2–4-mm size range (note that this actual crystal size space). For sizes less than 2 mm (greater than 4 mm), it is assumed that the size distribution is entirely composed of crystals (aggregates). The blending is done by determining the reflectivity weighted velocity contribution for aggregates and crystals by linearly increasing the aggregate concentration in the 2–4 mm size range. This produces one piecewise continuous fall speed–size relationship. Figure 2 displays the blended fall speed–size relationship using crystal mass–size and fall speed–size relationships from Heymsfield and Kajikawa (1987) along with aggregate mass–size and fall speed–size relationships from Locatelli and Hobbs (1974) and Langelben (1954).[1]

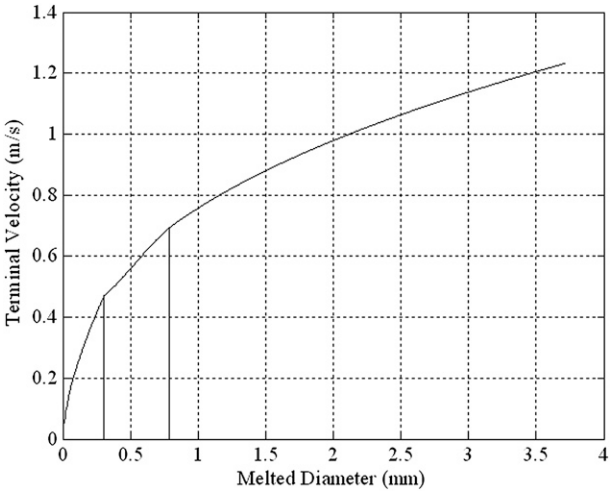

FIG. 2. An example of the continuous crystal to aggregate fall-speed relationship using the mass–size and fall speed–size relationships noted above. The two vertical lines indicate the melted diameters of the 2-mm crystal size and 4-mm aggregate size.

Second, spectral broadening as a result of same size snowflake fall speed variation was included. This is not performed for rainfall because terminal velocities of water drops follow published relationships to within $\pm 2\%$ (Atlas et al. 1973). For snowfall, Passarelli and Srivastava (1979) show significant fall speed deviations from the derived relationships. Sasyō and Matsuo (1985) also note that there can be significant fall speed variation for snowflakes of the same size. Therefore, a method to include the same size fall speed variation was developed following Passarelli and Srivastava (1979).

[1] Mass–size relationship from Heymsfield and Kajikawa (1987): $m = 6.12 \times 10^{-4} D^{2.29}$ (for dendritic crystals); and Locatelli and Hobbs (1974): $m = 3.7 \times 10^{-5} D^{1.4}$, where m is in grams, D in cm for the first relationship, and mm for second. Velocity–size relationship from Heymsfield and Kajikawa (1987): $v = 55\ D^{0.48}$ (for dendritic crystals); and Langelben (1954): $v = 178\ D^{0.372}$, where v is in cm s^{-1} and D in cm for both relationships.

This was done by assuming a size-dependent spread of possible velocities for a given snowflake size. As the snowflake size increased, the spread of possible fall speeds increased. Also, the range of fall speeds had more area toward faster fall speeds from the mean. This was done because an examination of Passarelli and Srivastava (1979, their Fig. 2) indicated that was the situation. The concentration of snowflakes was assumed to vary uniformly over that velocity interval, or a snowflake has an equal probability of having any velocity in the defined range for that size. This creates an increased precipitation spectral width as well as a larger mean fall velocity in the model spectrum, as shown by Fig. 3. This velocity spread for a given snowflake size should provide a more realistic representation of snowflake fall speeds than the fall speed–size relationship alone.

Once the model spectrum is created using the four-parameter set, it can be compared to the observed spectrum by minimizing a least squares function. Sato et al. (1990) define the chi-squared cost function to be minimized as

$$\chi^2 = \sum_{i=1}^{n} \left\{ \log[S_{\mathrm{obs}}(v_i)] - \log\left[S'(v_i)\right] \right\}^2, \qquad (10)$$

where S' is the model spectrum. When the spectral matching algorithm determines the parameters with the smallest χ^2, those parameters are assumed to be the correct solution. Methods to assess the uncertainty of this retrieval method will be discussed shortly. For details concerning the equations regarding the implementation of the chi-squared minimization, refer to Sato et al. (1990).

Sato et al. (1990) determined that it is better to limit the amount of points used in the χ^2 calculation to ± 20 spectral points around the maximum in the observed spectrum. This limit is imposed because outside of the main precipitation return spectrum, the algorithm is attempting to match random noise. This could lead to the search algorithm diverging, or convergence to a local minimum created by the noise pattern (i.e., an incorrect solution). For this work, the number of points used for matching was varied based on the signal-to-noise ratio. This is because spectra for snowfall have a smaller spectrum width than rainfall as a result of their reduced range of fall speeds. Also, in cases of low signal-to-noise ratios, the number of points above the noise can be very small, sometimes less than five. Because of this, the peak was selected and the points on both sides of the peak down to the noise level were selected, giving rise to the variable number of points to match. Figure 4 shows an example spectrum, with the precipitation peak delineated by the area between the two vertical black lines. Note the random noise fluctuations outside of the precipitation peak.

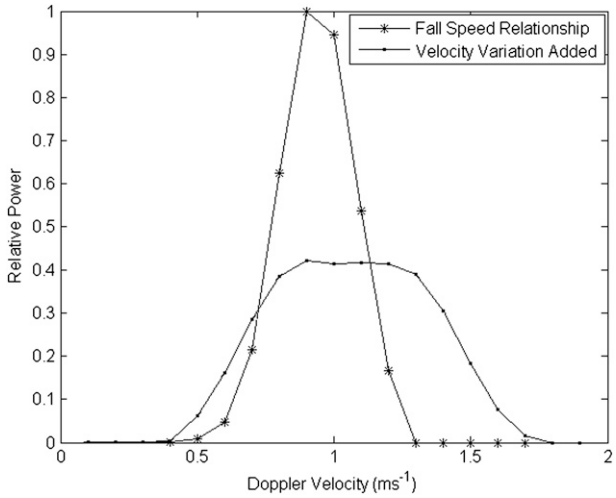

FIG. 3. Relative power values for a simulated profiler precipitation spectrum using the fall speed combination and same-size fall speed variation methods.

Because this work is using the least squares minimization (LM) method described by Sato et al. (1990) along with reflectivity and mean Doppler velocity constraints, the minimization involves two steps. In the first step, the LM method is given an initial guess of $\bar{w}$ and σ^2_{air}. The LM method then iterates until it converges to a solution at those specific $\bar{w}$ and σ^2_{air} values. The converged solution total reflectivity is then adjusted by varying N_0 to match the observed spectrum and χ^2 is recalculated. The algorithm then moves to the next ($\bar{w}$, σ^2_{air}) pair using the same initial guess for all ($\bar{w}$, σ^2_{air}) pairs. After all values of $\bar{w}$ and σ^2_{air} are tested, the second step of the minimization process determines the solution for this spectrum with the smallest χ^2 value and mean Doppler velocity difference. Overall, the underlying theory of the constraints and solution search is still similar to that of Williams (2002).

b. *Profiler calibration*

To produce absolute measurements of N_0, the profiler must be calibrated. Following the procedure described by Gage et al. (2000), the GRAO profiler was calibrated using DSD information from the SVI during a rainfall event in the summer of 2005. Calibration was performed only once because this type of profiler is very stable (Gage et al. 2000). Figure 5 displays the SVI and profiler-calculated reflectivity values for the section of the event used for calibration. Figure 5a shows a time series of the SVI and corrected profiler reflectivities. One can see good agreement throughout the entirety of the event

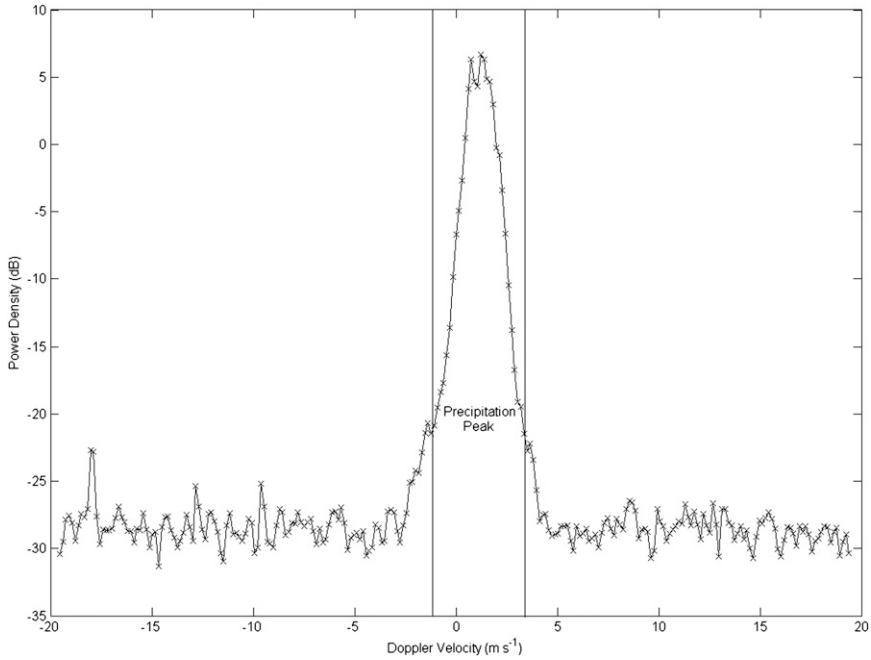

FIG. 4. An example profiler spectrum with the precipitation peak being the area between the two vertical black lines.

after the correction is applied. Figure 5b is a scatterplot of the profiler reflectivity versus the disdrometer reflectivity. Again, there is good agreement after the correction is made. Note the slope of the comparisons is nearly unity over a large range of reflectivities.

c. *Profiler retrieval performance*

1) UNCERTAINTY ANALYSIS

To determine the uncertainty of the profiler-derived SSDs, two experiments were selected with the first being simulations to determine the sensitivity of the profiler retrieval method to measurement uncertainty. Measurement uncertainty will cause errors between the observed and modeled spectrum because the modeled spectrum contains no noise. Measurement noise manifests itself as random fluctuations superimposed on the true spectrum. If one assumed the modeled spectrum was truth, there would be residual error as a result of the random noise. Because of this, the spectra matching method may provide erroneous results because χ^2 may be minimized at an incorrect location in parameter space as a result of measurement noise. To asses this inherent uncertainty, noisy simulated spectra were created following the methodology of Williams (2002).

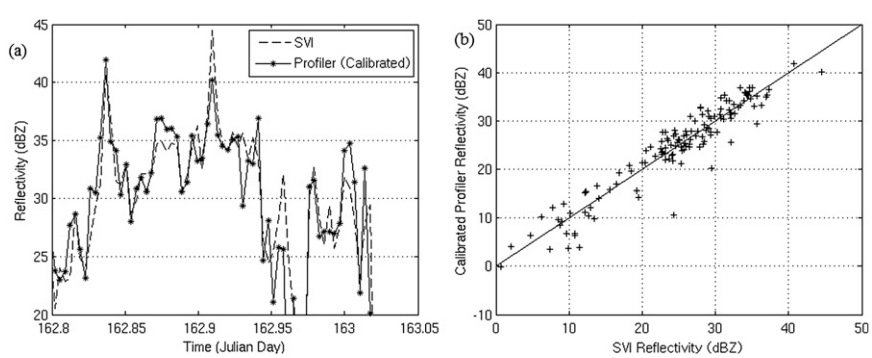

FIG. 5. (a) Time series of SVI and corrected profiler reflectivities and (b) a scatterplot of profiler reflectivity vs SVI-calculated reflectivity.

The spectra were produced over 10(N_0,Λ) pairs while holding $\bar{w}$ at zero and $\sigma_{\rm air}$ at five values: 0.1, 0.2, 0.4, 0.6, and 0.8 m s^{-1}. This was done to assess the ability of the spectra matching method under a range of conditions. The (N_0,Λ) pairs were taken from the range of values observed in this study. These ideal spectra then had random noise added to them at each spectral point. The random noise was generated using

$$\sigma(v) = \frac{S_{\rm obs}(v)}{\sqrt{\rm NFFT}}, \tag{11}$$

where NFFT is the number of independent velocity spectra averaged to form the observed reflectivity spectral density, and $\sigma(v)$ is the power density of the noise (Williams 2002). Then a point was randomly selected from a Gaussian distribution with a mean of zero and standard deviation given by Eq. (11) and used as the random noise at that spectral point. For each unique (N_0, Λ, $\bar{w}$, and $\sigma^2_{\rm air}$) point, 200 complete spectra were generated and run through the spectral matching method. The parameters of the distribution were calculated for each of the spectra. Median values and interquartile range were used as metrics to estimate the uncertainty of the retrieval process. These were chosen because the distributions of N_0 and Λ are highly skewed in some situations. Discussion of these results can be found in the appendix.

2) SVI COMPARISONS

Along with the measurement uncertainty sensitivity tests, comparisons of the lowest profiler gate SSDs to those of the SVI were made. This was done not only to estimate the performance of the spectra matching method but also to anchor the vertical profile of SSDs with a realistic surface point. Parameters of the exponential distribution were computed from the SVI and compared to those of the spectra matching method using the same performance metrics as discussed above. With the SVI serving as an anchor point, retrieved SSDs aloft can be qualitatively examined for coherence with the surface observations. Following some reasonable estimation of SSD evolution through the precipitating layer (Passarelli 1978; Lo and Passarelli 1982; and others), grossly incorrect SSDs could be identified and examined for possible error sources.

To compare the retrieved SSDs to the SVI observations, the maximum length SSD will need to be changed. Following the derivation of the equivalent reflectivity factor Z_e calculation in Smith (1984), the maximum length SSDs of the SVI will need to be scaled down to either melted diameter or ice sphere diameter distributions. Equivalent reflectivity factor is the radar reflectivity factor measured by the disdrometer converted to that measured by the profiler using the dielectric constant for water, which is denoted as Z. The calculation of Z_e from the disdrometer can be done by scaling the original SSD using an appropriate size–density or size–mass relationship for the original SSD (Magono and Nakamura 1965; Locatelli and Hobbs 1974; Heymsfield and Kajikawa 1987; Heymsfield et al. 2004). Given a density–size relationship, one could simply scale the original SSD by the factor

$$N(D_m) = N\left[D_s\left(\frac{\rho_i}{\rho_w}\right)^{1/3}\right], \tag{12}$$

where the subscript s denotes the original snowflake; D_m and D_s correspond to the melted diameter and ice diameter of the snowflake, respectively; ρ_i is the density of ice; and ρ_w is the density of water. In the case of a mass–size relationship, one only needs to convert the mass of the snowflake into the corresponding volume of water through

$$D_m = \left(\frac{6 \times {\rm Mass}_S}{\pi \times \rho_w}\right)^{1/3}, \tag{13}$$

where Mass$_S$ is defined as the mass of a given snowflake size. Once the original SSD has been scaled, it can be directly compared to estimated SSDs from the profiler. This process assumes that there is one unique density or mass for a given snowflake size, which will not be valid in many situations. For this paper, appropriate mass–size relationships from Locatelli and Hobbs (1974) and Heymsfield and Kajikawa (1987) were used. These were determined from the crystal habit information from the SVI. Examining the validity and errors of these specific assumptions are outside the scope of this work. With the instrumentation set available for this study, there is no proper way to assess the potential differences from the published relationships to what was occurring. Note that if the published relationship is incorrect, significant errors are possible.

Because of these errors clear a ''one mass–size relationship fits all'' methodology could introduce significant errors in the estimated melted equivalent SSD, even for the appropriate crystal habit. For example, subtle differences in aggregation or even component crystal size can result in different masses for the same size snowflake. A simple approach to account for some of this variation was developed by first identifying the main component crystal types for each event. From this, a mass–size relationship for the component crystals and

aggregates of those crystals was selected from previously published work. There are many different types of component crystals with more than 80 types present in the classification scheme developed by Magono and Lee (1966). Each component crystal type has a different mass–size relationship. Besides the relationships for component crystals, an aggregate composed of one crystal type will have a unique mass–size relationship as well. Therefore, it is important to have the best estimate of crystal type, so the appropriate mass–size relationships can be chosen from the literature. All relationships used here were power law relationships with the form

$$m = aL^b, \tag{14}$$

where m is the snowflake mass, and L is its maximum dimension. The coefficients a and b were empirically derived from observations. After the appropriate relationships were chosen, the a value for the aggregate relationship was modified until the calculated SVI reflectivity matched that of the profiler. Substituting Eq. (13) into the definition of equivalent radar reflectivity factor, one can see it is dependent on mass squared. Thus, using the maximum length SSD and assuming a 1:1 correspondence of mass to size for that SSD, the estimated masses using this method should be an improvement to the mass estimate.

Only the aggregate a value was changed because there are many uncertainties in applying mass–size relationships to different geographical areas with different storm dynamics. Because of this uncertainty and lack of many independent measurements, this simple method was used. Only varying the a coefficient is effectively translating the mass–size relationship left or right on a mass–size plot. Examination of the work done by Locatelli and Hobbs (1974) shows there is a high correlation coefficient (0.91) for the aggregate mass–size relationship used in this study. That fact supports the hypothesis that the exponent value may be constant for snowflakes with very similar component crystals. Also, the component crystal values were not modified because individual ice crystals make only small contributions to the overall reflectivity and equivalent rainfall rate values. This may introduce errors in fitting distribution parameters, but some assumptions and simplifications must be made to make this problem tractable. These errors are most likely small and of a smaller scale than instrumentation error sources and sampling concerns. These errors are expected to be less than 10% because the sizes of the melted diameters would only be slightly different if the component crystal density relationship were changed. Also, this changes only a few points in the observed spectrum, which will only account for a portion of the regression calculation.

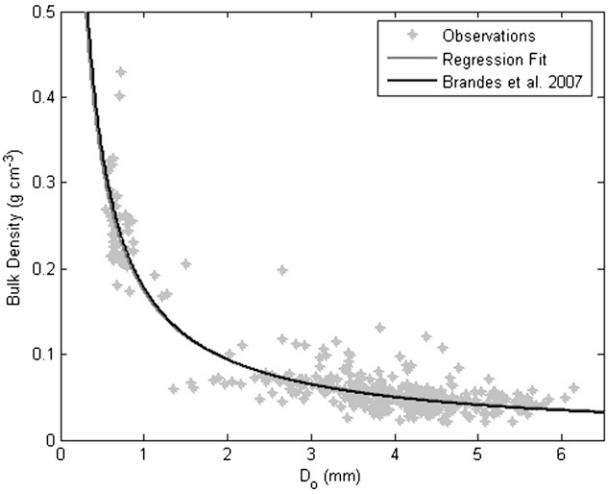

FIG. 6. Scatterplot of bulk density vs median volume diameter. Bulk density was estimated using the mass–size method discussed in the text while also assuming a spherical shape for aggregates and a cylindrical shape for individual crystals.

If the incorrect aggregate mass–size relationship is used, errors can become quite significant. With the current instrumentation setup, it is not entirely possible to estimate the correctness of these relationships. However, one attempt to check the validity of the current method was made by generating Fig. 6a from Brandes et al. (2007) for the events examined herein. Figure 6 gives the results from the mass–size determination method described above, using spherical snowflakes for the volume calculation. This figure is a scatterplot of estimated bulk density versus the median volume diameter (D_0). From Fig. 6 it can be seen that this study produces a nearly identical relationship to that of Brandes et al. (2007) along with minimal scatter around this relationship. This gives some confidence that the methods of estimating snowflake mass in this study are reasonable. In the future an independent estimate of liquid accumulation rate could provide an estimate of bulk density, similar to the method used in Brandes et al. (2007).

4. Results and discussion

Profiler retrievals

1) SURFACE RETRIEVALS

Retrievals of N_0 and Λ were made from the lowest gate (225 m AGL) of the GRAO profiler. Two slightly different methods were used to produce these retrievals, with the basic methodology discussed above used in both approaches. Also, both methods used the SVI SSDs as the initial guesses for the profiler retrieval algorithm.

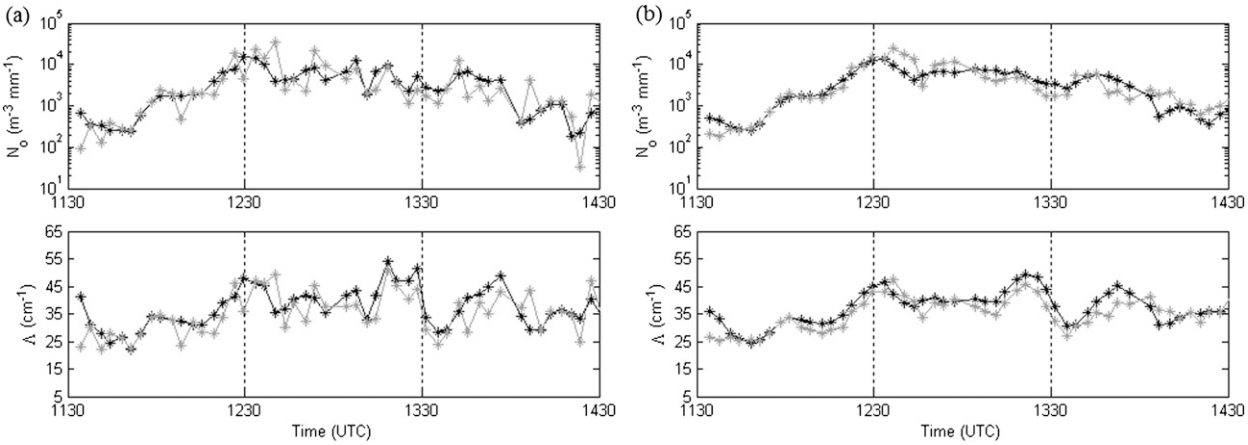

FIG. 7. Near-surface SSD parameters for event 3. (a) (top) Profiler-retrieved (gray line) and SVI (black line) N_0; (bottom) profiler-retrieved (gray line) and SVI (black line) Λ. (b) Three-point running average of (a).

These two slightly different approaches were developed to help improve the performance of the retrieval process by constraining the problem beyond the conservation of reflectivity and mean Doppler velocity.

The first method used a continuity approach to help constrain the problem. In stratiform precipitation, it is a common assumption that vertical velocities are small and fairly uniform in time and space. Therefore, $\bar{w}$ was only allowed to vary by ± 20 cm s^{-1} from one retrieval in time to the next. The retrievals occur every three minutes, so this constraint should be valid in most situations. Figure 7a displays the actual retrieved SSDs from the profiler (light gray line) and the SVI (black line), and Fig. 7b shows a three-point average applied to Fig. 7a for event 3 using the $\bar{w}$ constraint method. There is good agreement in both the raw and averaged data. The trends are matched by the profiler very well and there is little bias. Some oscillation is evident in the raw retrievals. This is caused by issues with the solution space and other possibilities that are discussed later.

The $\bar{w}$ constraint method did not perform as well as above for event 2 and event 4, so another constraint process was developed. The poor performance may be due to changes in the snowflake fall speeds being projected onto the $\bar{w}$ field. The second constraint method consisted of constraining the allowed N_0 and Λ values dependent on the profiler reflectivity. This uses the physical idea that more intense snowfall will have broader, lower intercept SSDs, which gradually shift to very narrow high intercept SSDs at very low intensity snowfall rates. As noted in the surface observations, this idea seems to be followed only loosely; therefore, the constraints were only applied loosely. Figures 8a,b display the surface profiler results for event 4 using the N_0–Λ constraint method. Again, there is oscillation in the raw solution of around one order of magnitude, which is quite significant. However, the trends are matched throughout the event, especially in the raw Λ retrievals. Applying the three-point average shows that there is very good agreement in this case as well. Closer inspection reveals that the oscillations tend to bracket the true solution, giving rise to the good agreement between averaged and observed values.

During most of event 5, the spectral width was very high, resulting from a significant amount of atmospheric turbulence. This was caused by the presence of a temperature inversion at approximately 1 km AGL along with speed and directional shear through the inversion. This lead to stronger clear-air returns because they are, in essence, dependent on the magnitude of atmospheric turbulence. With the small fall speeds of snowfall, the clear-air and precipitation returns can be superimposed on each other in many situations. The clear-air spectrum causes more power to be observed in the velocity gates on the left side of the precipitation peak or smaller particle area. This could cause the χ^2 minimum to reside in an area of higher N_0 and Λ. The surface retrievals shown in Figs. 9a,b from event 5 seem to indicate this is occurring. There is a distinct high bias in the retrieved SSD parameters from the profiler, which would be expected if the clear-air returns were influencing the observed spectrum enough to change the solution space. Again, there is general agreement between the profiler and SVI in both the raw and averaged retrievals. The oscillations in the raw data are again around an order of magnitude from point to point.

Overall, there were significant correlations between the profiler and SVI measurements for all five events, as shown in Table 1. Most of the scatter in the raw plots is due to the solution oscillations. This is also evident in

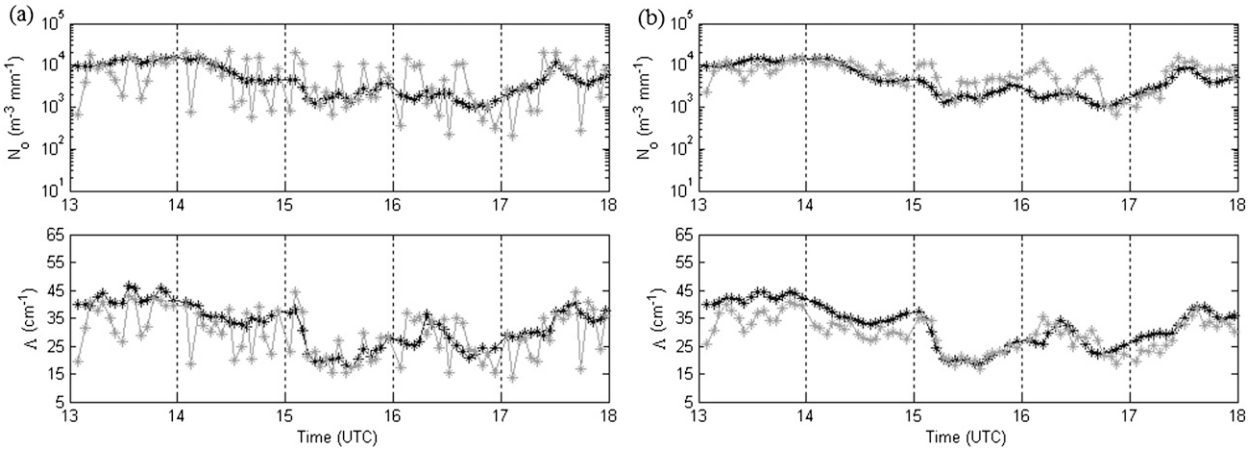

FIG. 8. Same as in Fig. 7, but for event 4.

Table 1 through the much lower correlation coefficients for the raw retrievals versus the averaged retrievals. For the averaged retrievals, all the events have correlations greater than 0.76 for Λ and greater than 0.43 for N_0. The lower correlations for N_0 correspond to the fact that for a given change in Λ, a much larger change in N_0 must be made to conserve reflectivity as a result of the D^6 dependence. The root mean squared error (RMSE) values are generally on the order of the SVI observations for N_0 except for event 1, where it is one to two orders of magnitude less. For Λ, the RMSE values are generally around 15%–30% of the observed values but only around 7% for event 1. Figure 10 shows scatterplots of N_0 and Λ for all five events. Again, the good general agreement between the retrievals and the observations is evident in the averaged retrievals, while the solution oscillation is evident in the raw retrievals.

The retrieval process oscillates around the correct solution. This oscillation relates back to the solution space, which is discussed in the appendix. Also, strong clear-air returns can influence the solution. The clear-air peak was not estimated for any of these results, but future work may investigate that possibility. It may lead to improved results in events similar to event 5 herein, if a robust way to estimate the clear-air return power can be developed. Rajopadhyaya et al. (1994) performed some basic SSD retrievals above the bright band using a VHF profiler and concluded that the uncertainty is higher than for rainfall and also increases quickly as the clear-air spectral width increases. Their conclusions are supported by the surface results presented above. Event 1 had the highest correlations and lowest relative RMSE of any of the events, and it also had the smallest spectral widths. The other events had lower correlations, larger

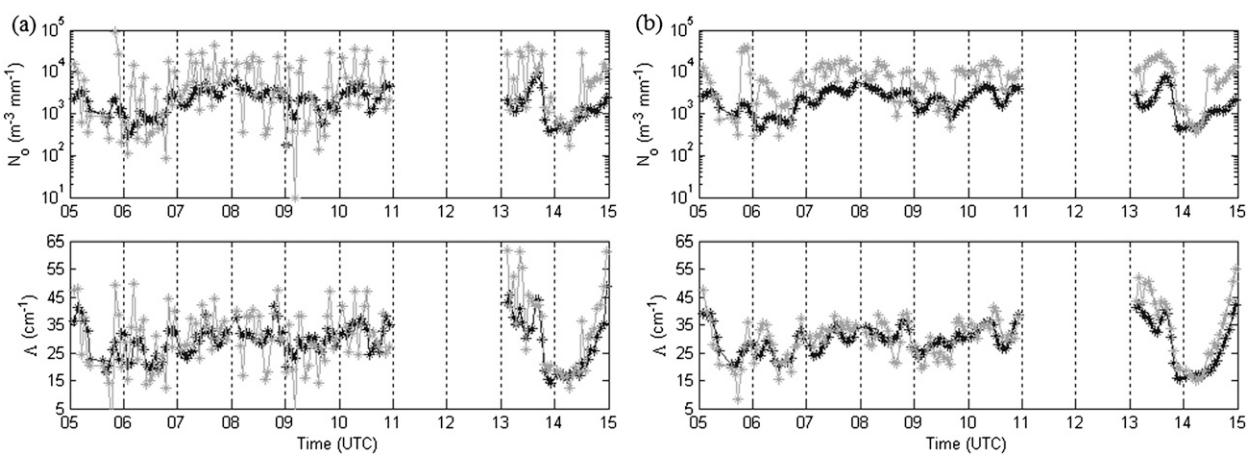

FIG. 9. Same as in Fig. 7, but for event 5.

TABLE 1. Correlation coefficient, bias, RMSE, and RMSE with the bias removed for the five events at the 225-m range gate. Bias, RMSE, and zero bias RMSE were only calculated for the averaged retrievals.

	Correlation coef		Bias		RMSE		RMSE no bias	
	N_0	Λ	N_0 (m^{-3} mm^{-1})	Λ (cm^{-1})	N_0 (m^{-3} mm^{-1})	Λ (cm^{-1})	N_0 (m^{-3} mm^{-1})	Λ (cm^{-1})
Event 1								
Raw	0.99	0.95	—	—	—	—	—	—
Avg	0.99	0.97	2.0e5	6.6	3.4e5	9.4	2.8e5	6.6
Event 2								
Raw	0.41	0.59	—	—	—	—	—	—
Avg	0.59	0.76	850	0.4	1.9e3	4.0	1.7e3	4.0
Event 3								
Raw	0.54	0.68	—	—	—	—	—	—
Avg	0.79	0.84	674	−2.1	3.3e3	3.9	3.3e3	3.4
Event 4								
Raw	0.44	0.61	—	—	—	—	—	—
Avg	0.67	0.84	1.0e3	−1.0	3.6e3	5.0	3.3e3	4.0
Event 5								
Raw	0.27	0.66	—	—	—	—	—	—
Avg	0.43	0.81	6.3e3	1.8	9.1e3	5.4	6.7e3	5.1

relative RMSE, and larger spectral widths. In spite of these issues and uncertainties, the retrieval process seems to be producing physically reasonable results.

A consistency check of the near-surface profiler retrievals was performed using the next highest range gate, which was 315 m AGL. A summary of the retrieval performance for these retrievals is given in Table 2. These results show that the profiler retrieval algorithm performed better for events 1, 3, 4, and 5, with a slight decrease in performance for event 2. This may be due to SSD evolution during event 2, or as a result of solution oscillation problems. The performance increases for the other four events may indicate some ground clutter issues or more turbulent broadening near the surface. The

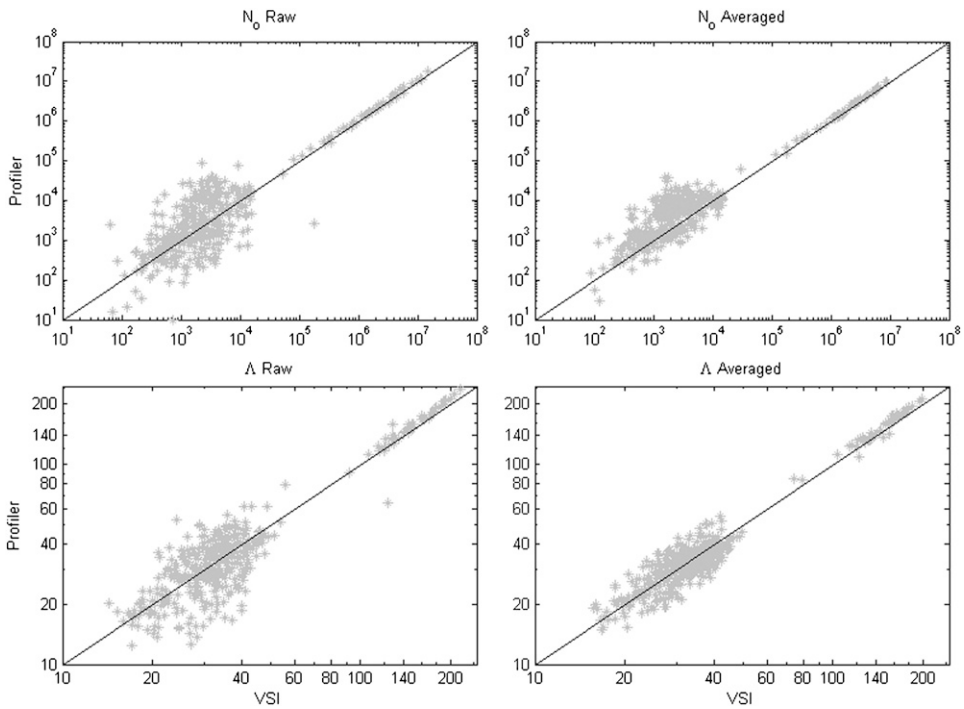

FIG. 10. Scatterplots of (top) N_0 and (bottom) Λ for (left) the raw and (right) averaged values for the five events. Note that Λ is plotted in log space to condense the retrieval values.

TABLE 2. Same as in Table 1, but for the 315-m range gate.

	Correlation coef		Bias		RMSE		RMSE no bias	
	N_0	Λ	N_0 (m^{-3} mm^{-1})	Λ (cm^{-1})	N_0	Λ	N_0 (m^{-3} mm^{-1})	Λ (cm^{-1})
Event 1								
Raw	0.99	0.96	—	—	—	—	—	—
Avg	0.99	0.99	1.1e5	3.6	2.3e5	6	2.0e5	4.8
Event 2								
Raw	0.31	0.51	—	—	—	—	—	—
Avg	0.48	0.67	4.0e3	0.5	1.0e4	6.2	9.3e3	6.2
Event 3								
Raw	0.61	0.68	—	—	—	—	—	—
Avg	0.79	0.89	62	−1.5	2.0e3	3.3	2.0e3	2.9
Event 4								
Raw	0.59	0.87	—	—	—	—	—	—
Avg	0.81	0.96	1.9e3	−1.1	3.8e3	2.4	3.3e3	2.1
Event 5								
Raw	0.39	0.69	—	—	—	—	—	—
Avg	0.49	0.81	830	−1.3	2.4e3	4.0	2.2e3	3.8

fact that the retrieval process performs similarly at the next range gate gives more confidence that this process is producing physically realistic results and that ground clutter contamination in the lowest gate is most likely negligible for these events. Examination of actual spectra at the lowest gate shows they are very similar to the second gate. Therefore, we believe the use of the lowest gate for comparison purposes is acceptable in this situation.

2) VERTICAL RETRIEVALS

Vertical profiles of SSDs could be made using either method outlined above with a constant initial guess, or using the retrieval from the previous lower height as the initial guess. Typically, retrievals are able to be made up to 2–3 km above ground with the possibility of some cases having retrievals more than 3 km in height. The main limiting factor of the retrieval height is that snowfall is typically shallow with low reflectivity values (<10 dBZ) above 2 km, and the profiler sensitivity decreases with height. This creates low signal-to-noise ratios in these areas, resulting in spectra with peaks having five or fewer points above the noise. Even with these limiting factors, profiles of SSDs can be produced throughout the precipitating layer in a majority of the profiles in these cases. Note that the fall speed relationships used in the retrieval algorithm have been corrected for altitude using the method of Foote and Du Toit (1969).

An example profile of Z_e along with the retrieved N_0 and Λ from the profiler from event 2 during the passage of a convective band are given in Fig. 11. Immediately noticeable is that the raw vertical retrievals are influenced by the same oscillations as the lowest gate retrievals because of oscillations in the solutions. Again, a three-point running average was applied to the data to remove some of these oscillations. Even in the raw data, a general trend of increasing N_0 and Λ with height is seen, with reflectivity decreasing over that same distance. The trend of increasing N_0 and Λ with height is physically realistic, especially in areas of decreasing reflectivity with height. In general, decreasing reflectivity corresponds to higher N_0 and Λ values at the surface, which should hold in the vertical as well. Also, SSD observations from airplane studies also show an increase of N_0 and Λ with height through the precipitation layer (Lo and Passarelli 1982).

From a microphysics standpoint, this is the expected outcome. Above the precipitation layer, ice crystals are formed, grow through deposition, and slowly descend through the cloud. As they continue lower in the cloud, growth through aggregation occurs and begins to dominate the evolution of the SSD through the layer observed by the profiler. The aggregation process produces larger and larger snowflakes as smaller snowflakes combine as they fall, which corresponds to an increase in the reflectivity observations. This process broadens the SSD through the generation of larger snowflakes and reduces N_0 because aggregation collects many individual ice crystals (Passarelli 1978; Passarelli and Srivastava 1979; Lo and Passarelli 1982; Sasyō and Matsuo 1985).

A vertical profile taken from event four during the heavy snowfall band is given in Fig. 12. The reflectivity profile shows reflectivities greater than 25 dBZ_e to about 1.5 km in height. In the lowest 800 m, the reflectivity profile is nearly constant with height along with the retrieved N_0–Λ profile. This is implying that the

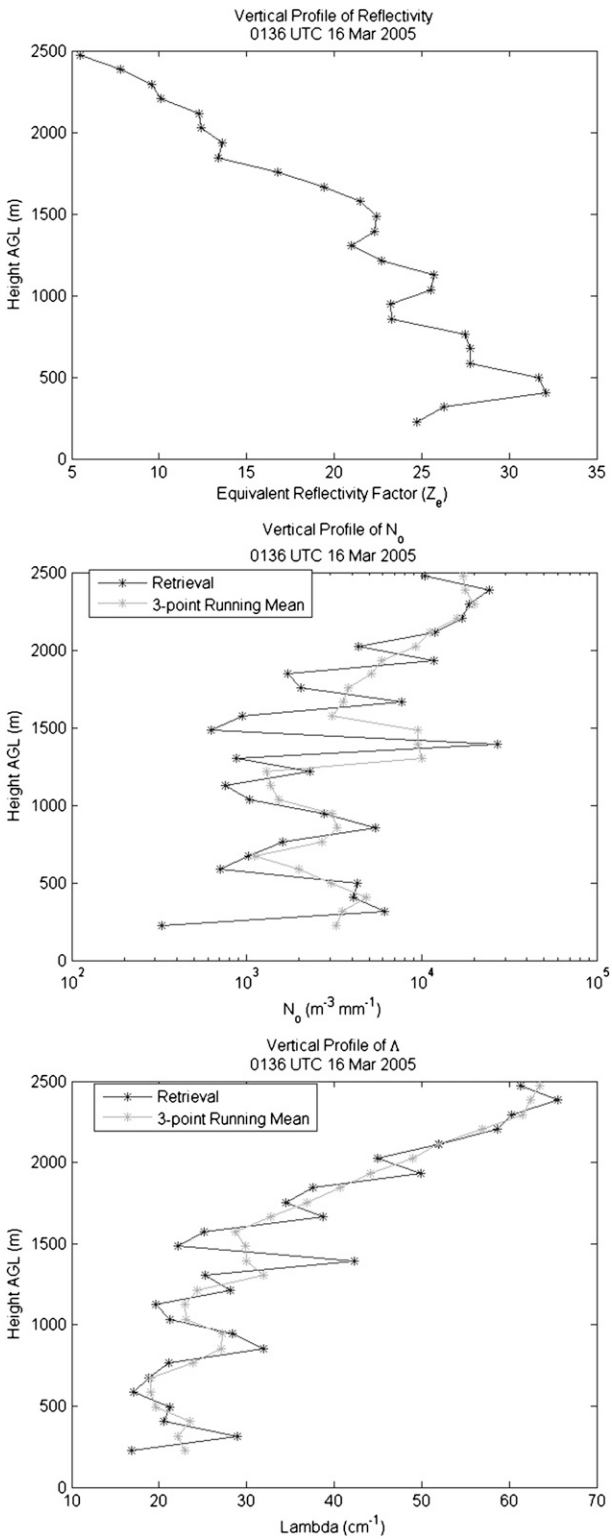

FIG. 11. Vertical profiles of (top) reflectivity along with retrieved estimates of (middle) N_0 and (bottom) Λ for a profile during event 2.

SSD is not undergoing any net evolution with height, or that equilibrium has been reached. Equilibrium SSDs in snowfall have been observed in airplane studies in the past (Lo and Passarelli 1982), suggesting this retrieval is physically realistic. Above this equilibrium layer, there is a gradual increase in both N_0 and Λ through the depth of the profile. Again, moving upward through the snowfall, this is physically expected.

A final example of an observed vertical profile from event 5 is shown in Fig. 13. This profile is similar to the profile from event 4, except with larger oscillations. Ignoring the four points that seem to be severe outliers, a nearly equilibrium layer below 800 m is, again, evident. The large outliers evident in event 5 occur because there is an increase in spectral broadening due to increased air turbulence. Large values of spectral broadening increase the retrieval uncertainty, as discussed in the appendix. Gradual increase in N_0 and Λ with height above that level is also retrieved. As in the prior cases, this profile seems to be physically realistic based on the reflectivity profile and the physical expectations of SSD evolution in snowfall.

The physical realism of these three profiles gives confidence that the profiler retrieval algorithm is functioning properly. Prior SSD observations from airplanes agree with these results as well, giving further confidence that there is useful information being produced. The use of a vertical profiler in this way provides the ability to produce many vertical profiles for many different types of snowfall. The oscillations in the retrievals present some problems. It is highly likely that some smoothing will be acceptable for satellite GV purposes but that is not examined here. Validation of the vertical profiles through the use of aircraft observations needs to be performed whenever possible. Overall, vertical profiles produced using this methodology and instrumentation should be a useful tool for satellite GV in the future.

5. Conclusions and future directions

In conjunction with the video snow imager (SVI), a 915-MHz profiler was used to provide near-surface and vertical profiles of snow size distributions (SSDs). Model spectra are produced and the least squares minimization (LM) method is used to minimize χ^2, which objectively determines the best-fit model spectrum to the observations. The best solution is determined after adding constraints requiring the moments of reflectivity and mean Doppler velocity for both the model and the observed spectra to be consistent (Williams 2002). Because snowfall has more complex relationships between velocity, density, and size than rainfall, two modifications

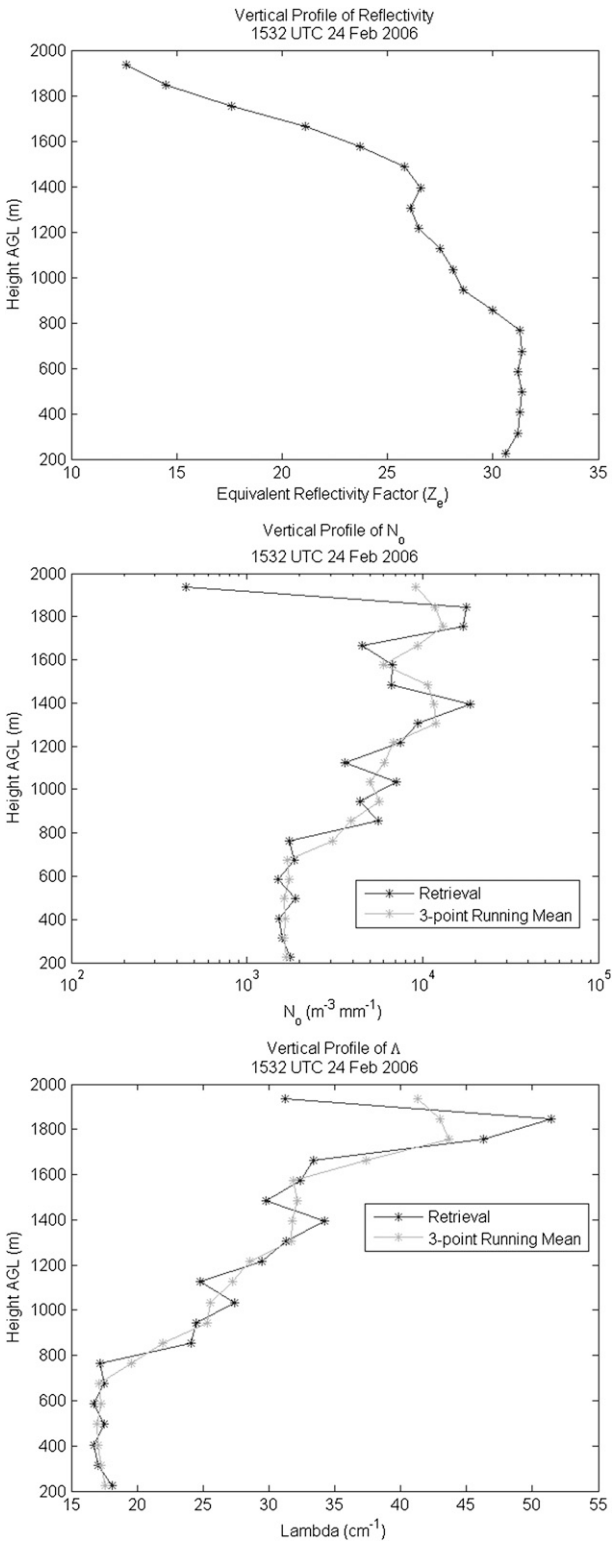

FIG. 12. Same as in Fig. 11, but for event 4.

to the profiler rainfall retrieval methods discussed in the literature were made. The first one was the use of a blended fall speed–size relationship. An ice crystal and aggregate fall speed relationship were used to completely describe the fall speeds of the observed spectrum. The second modification was the inclusion of same size fall speed variation. It has been shown (Passarelli and Srivastava 1979) that snowflakes of the same size have a nonnegligible range of fall speeds. Therefore, a method to include this fall speed variation was included in the calculation of the model spectrum.

For this study, 24 h of snowfall (broken up into five events) were selected to provide the initial evaluation of the profiler retrieval algorithm. Lowest gate (225 m AGL) profiler retrievals were performed for all five events of snowfall and compared to the SVI to determine if this retrieval process would provide reasonable results. Overall, it was found that the retrieval process agrees with the SVI observations quite well when some type of smoothing is applied to the data. Temporal smoothing was required because the individual retrievals have an oscillation of about one order of magnitude for N_0 and around 15%–30% for Λ. The correlation coefficient for N_0 ranged between 0.43 and 0.99 and between 0.76 and 0.97 for Λ for the five events. A consistency check using the next highest gate (315 m AGL) showed slightly improved but overall very similar results as the lowest gate retrievals. The improvements may be due to a reduction in ground clutter contamination. To help improve the retrieval process, two types of constraints were developed. The first method constrains the amount of temporal variation in $\bar{w}$ from profile to profile. This follows the idea that during stratiform precipitation, such as snowfall, there should be minimal variation in $\bar{w}$ during a span of three minutes. The second method loosely constrains the valid N_0 and Λ values. Using some expected value range for the given snowfall conditions, namely, reflectivity, the possible N_0 and Λ can be reduced to a more realistic range.

Example vertical profile retrievals showed that the retrieval algorithm appears to produce physically realistic results. The vertical profiles were determined using the same retrieval processes as the lowest gate retrievals and have similar oscillations as well. Smoothed profiles using a three-point running average generally show increasing N_0 and Λ with height in the precipitation layer, which was found by Lo and Passarelli (1982). The retrievals also show what appears to be an equilibrium SSD layer near the surface, which was also observed by Lo and Passarelli (1982). Validation of the vertical profiles through coincident aircraft observations is needed.

During the uncertainty analysis, an examination of the solution space revealed a possible explanation for

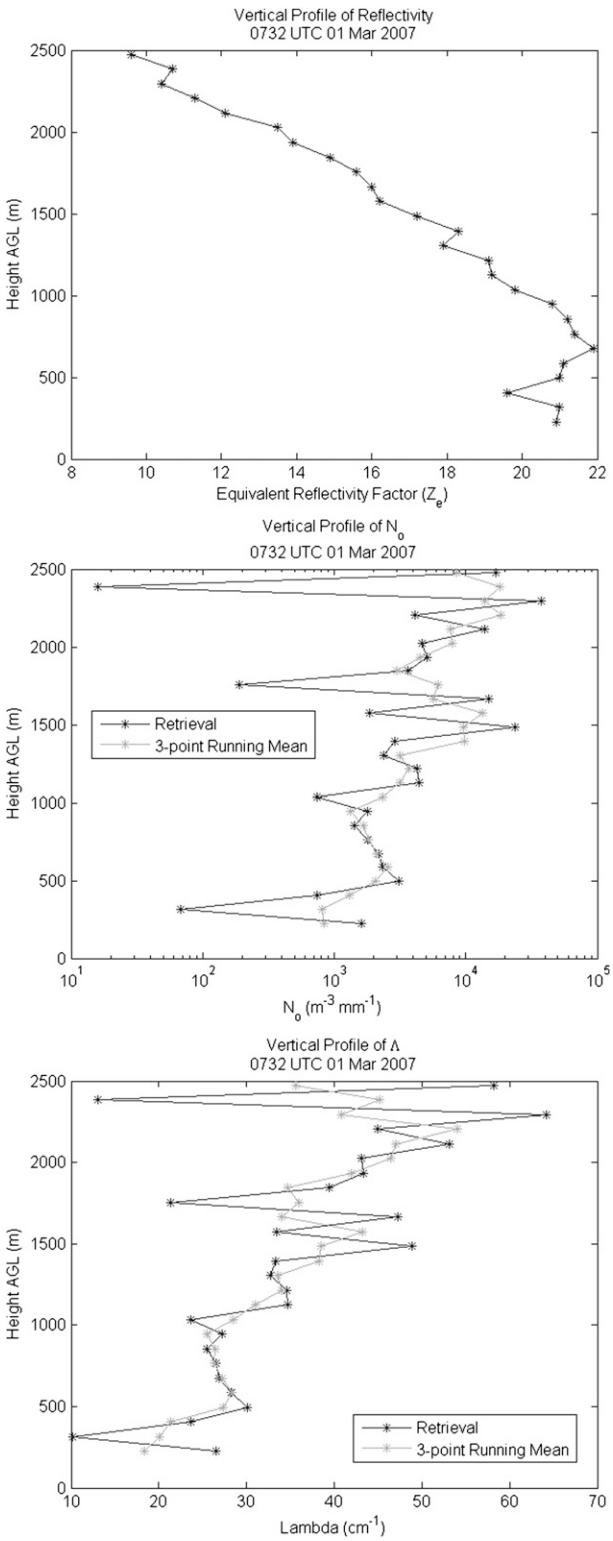

FIG. 13. Same as in Fig. 11, but for event 5.

the oscillations seen in the retrievals. The solution space in the N_0–Λ plane is ill-defined because it has a large valley of very similar χ^2 values. This is because the observed spectrum is typically very symmetric and that large changes in the SSD parameters result in small variations in the observed Doppler spectrum and its moments. The extent of the χ^2 valley agrees well with the observed magnitudes of the oscillations. Also, 200 simulated noisy spectra were produced for 10 different SSDs over air turbulence values ranging from 0.1 to 0.8 m s^{-1} to provide further uncertainty bounds to the retrieval algorithm. These results showed that as the air turbulence increases, so does the uncertainty. Also, the uncertainties associated with snowfall retrievals are higher than for rainfall (Rajopadhyaya et al. 1994; Williams 2002). It was also shown that narrow SSDs have lower uncertainty than broad SSDs in almost all cases.

The initial development of a methodology to retrieve SSD information from a 915-MHz profiler has produced very reasonable results. Now that a basic understanding of the process exists, a more detailed examination of this process can be undertaken. Producing improved constraints to more precisely define the solution space should be examined. Different ways to present the solution space may provide a more distinct answer. It is possible that using a different metric instead of χ^2 or a combination of χ^2 and along with some other constraint may provide a well-behaved solution space. Changes in the profiler operating parameters to increase the Doppler velocity spectral resolution may improve the retrieval performance as well. Another possibility may come from a less deterministic solution approach. Using the uncertainty analysis in the appendix, probability density function could be provided at every height that would give an estimate of the most likely SSD as well as the uncertainty associated with that estimate. This route may prove to be the more valuable option for validating satellite retrieval algorithms.

Last, instrument changes and improvements could be made in light of this initial study. The addition of independent measurements of snowflake mass and fall-velocity estimates would improve the uncertainty estimates of the inputs to the profiler retrieval algorithm. This could be done with the use of another type of distrometer (i.e., 2DVD) and a Genor weighting precipitation gauge, as in Brandes et al. (2007). It would also be advantageous to have a record of crystal type as another piece of information. This could eventually be related to different SSDs and vertical evolution in a statistical study. A smaller beamwidth profiler, possibly using a higher frequency (i.e., S band), could help lessen turbulent broadening issues as well as reduce Bragg scattering

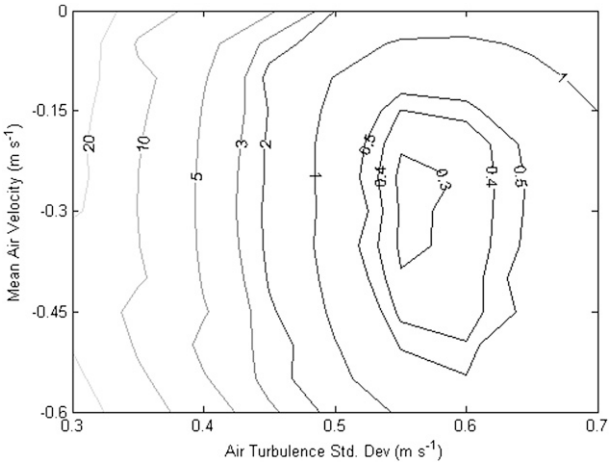

FIG. A1. Contours of χ^2 in the $\bar{w}$– $\sigma_{\rm air}$ plane for a lowest gate retrieval from event 5.

returns. Overall, this paper has provided a useful first step toward developing a methodology to retrieve surface and vertical profiles of SSDs over many winter seasons.

APPENDIX A

Uncertainty Analysis

a. Solution space

The profiler retrieval algorithm seems to oscillate around the observations by around an order of magnitude in most situations. Examination of the χ^2 topography, or solution space, revealed that it is not well behaved. Figure A1 displays a contour map of χ^2 in the $\bar{w}$– σ_{air} plane for an example surface retrieval taken from event 5. The solution space in this plane is well behaved because it has one minimum, and all areas around the minimum lead the search to that point. If χ^2 were used as a proxy for height, the minimum would be a very small valley with the slope leading upward in every direction out of the minimum.

When examining the solution space in the N_0–Λ plane, the reasons for the solution oscillations become apparent. Figure A2 gives the solution space in the N_0–Λ plane at the $\bar{w}$–σ_{air} minimum for the same example as in Figure A1. Lines of constant mean Doppler velocity

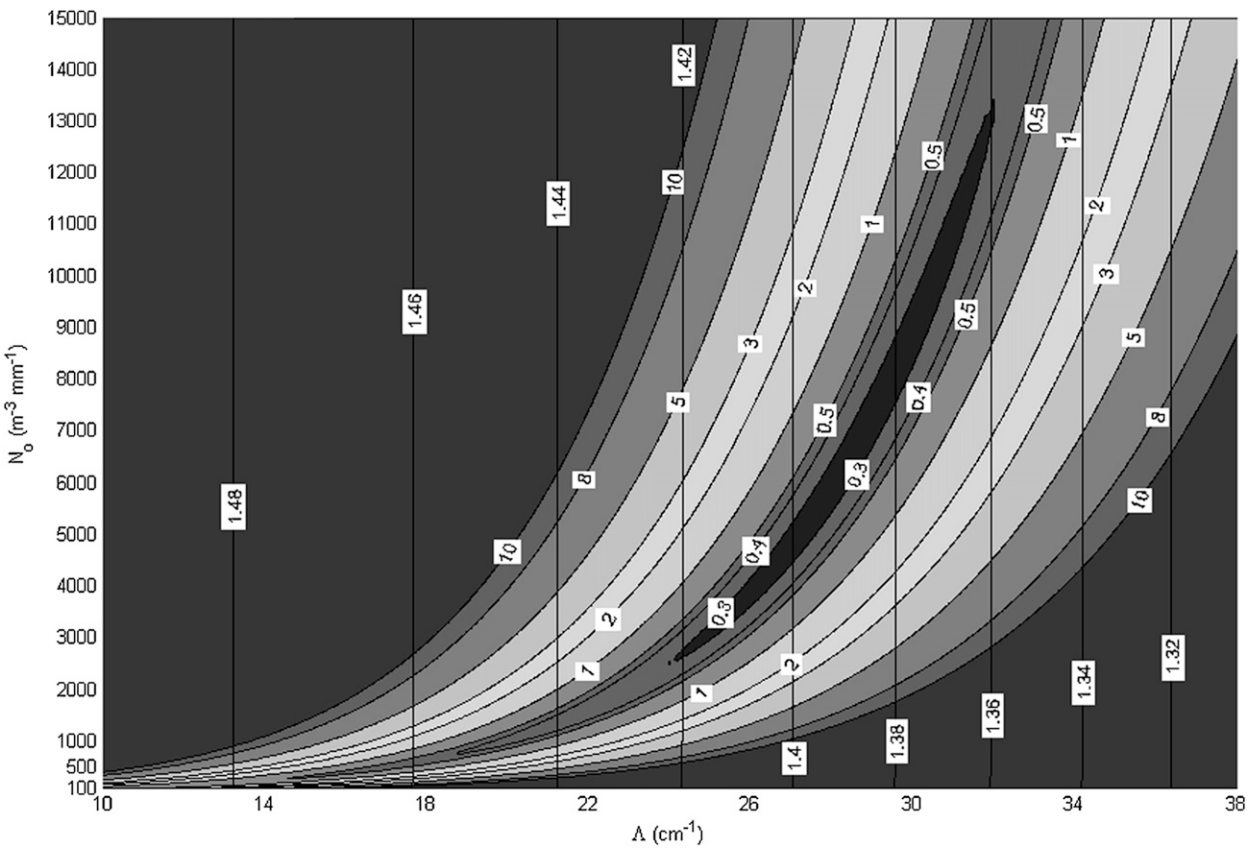

FIG. A2. Contours of χ^2 in the N_0–Λ plane at the $\bar{w}$– $\sigma_{\rm air}$ minimum for the example given in Fig. A1. Lines of constant mean Doppler velocity (m s^{-1}) are in black.

TABLE A1. The 10 SSDs used in the uncertainty analysis.

SSD	1	2	3	4	5	6	7	8	9	10
N_0	10^6	10^5	10^4	5×10^3	5×10^3	2×10^3	10^3	10^3	5×10^2	10^2
Λ	180	120	38	40	30	25	18	20	15	22

(m s^{-1}) are given in black. From this contour plot, it can be seen that while the solution space funnels toward one minimum, the minimum area is a broad valley. This is an area that has very small changes in χ^2 over a large area of parameter space. Following a χ^2 contour, the 0.3 line, for example, gives a range of possible N_0 values spanning just more than one order of magnitude and Λ values spanning a range of 8 cm^{-1}. These values correspond very closely to the RMSE errors listed in Table A1 for and the visual estimation of solution oscillations from Figs. 5–7. It is also worthwhile to note that over this χ^2 valley, the mean Doppler velocity varies by about 6 cm s^{-1}. Using the noise simulations outlined in the methodology section, the standard deviation in mean Doppler velocity from random noise is anywhere from 2–6 cm s^{-1}, depending on the SSD.

The solution behavior arises from the inherent properties of snowfall, rather than properties of the minimization method. Because the fall speed range of snowfall is very narrow, large changes in the distribution parameters result in small changes in observed Doppler spectra and their corresponding moments. This results in a nonuniqueness issue. Using χ^2 and the moment constraints still leave a large area of parameter space open to consideration as a valid solution because of instrumentation uncertainties. This is why the continuity and SSD parameter constraint methods were developed.

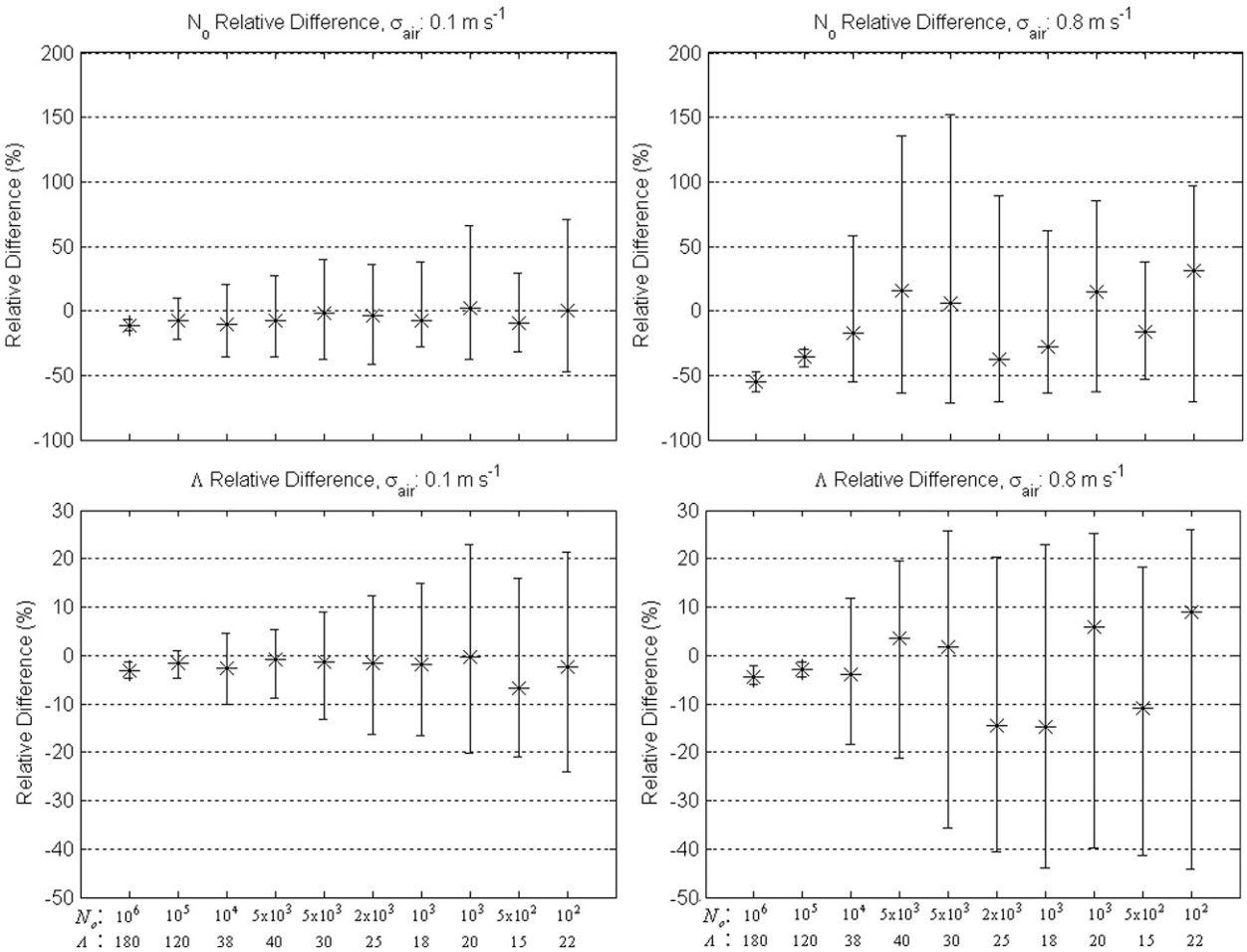

FIG. A3. Relative differences for (top) N_0 and (bottom) Λ for the 10 SSDs at σ_{air} values of (left) 0.1 and (right) 0.8 m s^{-1}.

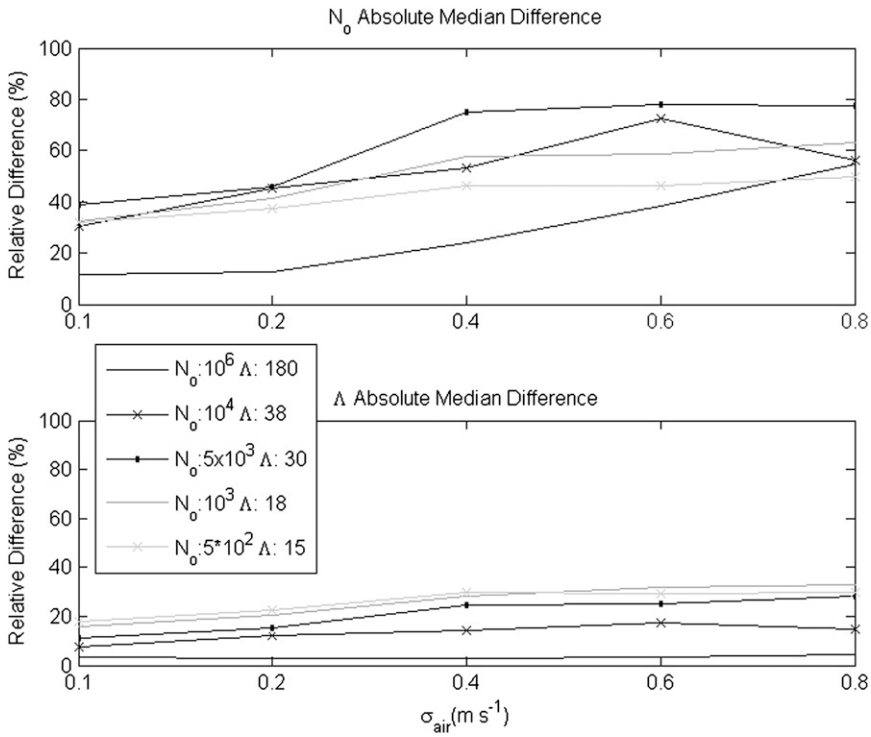

FIG. A4. Absolute median difference values for (top) N_0 and (bottom) Λ for 5 of the 10 SSDs over all of the σ_{air} values.

b. Simulated spectra

To help to understand the behavior of this retrieval process further, an uncertainty analysis similar to that of Williams (2002) was performed. Ten different SSDs, summarized in Table A1, were simulated over five different σ_{air} values [see Eq. (2)], with σ_{air} values ranging from 0.1 to 0.8 m s^{-1}. Relative differences and interquartile ranges for σ_{air} values of 0.1 and 0.8 m s^{-1} are given in Figure A3. The retrieval process has a larger uncertainty in the more turbulent case, which agrees with Rajopadhyaya et al. (1994) and rainfall studies (Williams 2002). The interquartile range of uncertainties shown here are up to 150% for N_0 and 40% for Λ. These values are smaller than those reached using actual data and comparisons to the SVI for N_0 and of the same order for Λ. It is expected that these simulations have smaller uncertainties than comparisons to another type of instrument as a result of sampling differences—instrument uncertainty in the SVI along with uncertainties in the assumed density relationship used for the retrieval process. The reason the Λ uncertainties here are similar is that the RMSE values above were computed using the averaged data, which will reduce some of the uncertainty in that case. Also the fact that Λ is less sensitive to slight changes in the observed spectra than N_0 may result in less uncertainty in observed data cases.

The absolute median relative differences for five of the simulated SSDs over the range of air turbulence values are shown in Figure A4. Absolute median relative difference is the value at which half of the simulated retrievals had larger absolute percentage differences than shown here and half had smaller absolute percentage differences. The SSD values used to generate the noisy spectra are shown in the legend. Again, this plot shows that uncertainty increases as air turbulence increases. It also shows that narrow SSDs generally have less uncertainty than broader SSDs. This is why the profiler retrievals performed so well in event 1. It consisted of narrow SSDs with minimal air turbulence.

The general uncertainty trends seen for rainfall seem to apply to snowfall based on this uncertainty analysis and the results from the profiler to SVI comparisons. As the air turbulence increases, the uncertainty of the retrieval increases. The uncertainty for snowfall is also larger than that for rainfall, which agrees with Rajopadhyaya et al. (1994). Examination of the solution space reveals that there is a valley of similar solutions that spans slightly more than an order of magnitude of possible values for N_0 and a large range of Λ values 6–10 cm^{-1}. This results in the need for constraints beyond conservation of reflectivity and mean Doppler velocity in the retrieval process.

Acknowledgments. The authors would like to thank Paul Johnston and Dave Carter for their technical expertise concerning the profiler. This work was supported by NASA Headquarters under the NASA Earth and Space Science Fellowship program, Grant NNG04GQ08H.

REFERENCES

Atlas, D., R. S. Srivastava, and R. S. Sekhon, 1973: Doppler radar characteristics of precipitation at vertical incidence. *Rev. Geophys.,* **11,** 1–35.

Barthazay, E., S. Göfke, R. Schefold, and D. Högl, 2004: An optical array instrument for shape and fall velocity measurements of hydrometeors. *J. Atmos. Oceanic Technol.,* **21,** 1400–1416.

Battan, L. J., and J. B. Theiss, 1966: Observations of vertical motions and particle sizes in a thunderstorm. *J. Atmos. Sci.,* **23,** 78–87.

Brandes, E. A., K. Ikeda, G. Zhang, M. Schönhuber, and R. Rasmussen, 2007: A statistical and physical description of hydrometeor distributions in Colorado snow storms using a video disdrometer. *J. Appl. Meteor. Climatol.,* **46,** 634–650.

Caton, P. G. F., 1966: Raindrop-size distributions in the free atmosphere. *Quart. J. Roy. Meteor. Soc.,* **92,** 15–30.

Currier, P. E., S. K. Avery, B. B. Balsley, K. S. Gage, and W. L. Ecklund, 1992: Combined use of 50 MHz and 915 MHz wind profilers in the estimation of raindrop size distributions. *Geophys. Res. Lett.,* **19,** 1017–1020.

Foote, G. B., and P. S. Du Toit, 1969: Terminal velocity of raindrops aloft. *J. Appl. Meteor.,* **8,** 249–253.

Gage, K. S., C. R. Williams, W. L. Ecklund, and P. E. Johnston, 1999: Use of two profilers during MCTEX for unambiguous identification of Bragg scattering and Rayleigh scattering. *J. Atmos. Sci.,* **56,** 3679–3691.

——, ——, P. E. Johnston, W. L. Ecklund, R. Cifelli, A. Tokay, and D. A. Carter, 2000: Doppler radar profilers as calibration tools for scanning radars. *J. Appl. Meteor.,* **39,** 2209–2222.

Gossard, E. E., 1988: Measuring drop-size distributions in clouds with a clear-air-sensing Doppler radar. *J. Atmos. Oceanic Technol.,* **5,** 640–649.

——, 1994: Measurement of cloud droplet spectra by doppler radar. *J. Atmos. Oceanic Technol.,* **11,** 712–726.

——, and R. G. Strauch, 1983: *Radar Observation of Clear Air and Clouds*. Elsevier, 280 pp.

Gunn, K. L. S., and J. S. Marshall, 1958: The distribution with size of aggregate snowflakes. *J. Meteor.,* **15,** 452–466.

Hauser, D., and P. Amayenc, 1981: A new method for deducing hydrometeor-size distributions and vertical air motions from Doppler radar measurements at vertical incidence. *J. Appl. Meteor.,* **20,** 547–555.

——, and ——, 1983: Exponential size distributions of raindrops and vertical air motions deduced from vertically pointing Doppler radar data using a new method. *J. Climate Appl. Meteor.,* **22,** 407–418.

Heymsfield, A. J., and M. Kajikawa, 1987: An improved approach to calculating terminal velocities of plate-like crystals and graupel. *J. Atmos. Sci.,* **44,** 1088–1099.

——, A. Bansemer, C. Schmitt, C. Twohy, and M. R. Poellot, 2004: Effective ice particle densities derived from aircraft data. *J. Atmos. Sci.,* **61,** 982–1003.

Langelben, M. P., 1954: The terminal velocity of snowflakes. *Quart. J. Roy. Meteor. Soc.,* **80,** 174–181.

Lo, K. H., and R. E. Passarelli, 1982: The growth of snow in winter storms: An airborne observational study. *J. Atmos. Sci.,* **39,** 697–706.

Locatelli, J. D., and P. V. Hobbs, 1974: Fall speeds and masses of solid precipitation particles. *J. Geophys. Res.,* **79,** 2185–2197.

Magono, C., and T. Nakamura, 1965: Aerodynamic studies of falling snowflakes. *J. Meteor. Soc. Japan,* **43,** 139–147.

——, and C. W. Lee, 1966: Meteorological classification of natural snow crystals. *J. Fac. Sci. Hokkaido Univ. Ser. 7,* **2,** 320–325.

Newman, A. J., P. K. Kucera, and L. F. Bliven, 2009: Presenting the snowflake video imager (SVI). *J. Atmos. Oceanic Technol.,* **26,** 167–179.

Passarelli, R. E., 1978: Theoretical and observational study of snow-size spectra and snowflake aggregation efficiencies. *J. Atmos. Sci.,* **35,** 882–889.

——, and R. C. Srivastava, 1979: A new aspect of snowflake aggregation theory. *J. Atmos. Sci.,* **36,** 484–493.

Rajopadhyaya, D. K., P. T. May, and R. A. Vincent, 1993: A general approach to the retrieval of raindrop size distributions from wind profiler Doppler spectra: Modeling results. *J. Atmos. Oceanic Technol.,* **10,** 710–717.

——, ——, and ——, 1994: The retrieval of ice particle size information from VHF wind profiler Doppler spectra. *J. Atmos. Oceanic Technol.,* **11,** 1559–1568.

——, ——, R. C. Cifelli, S. K. Avery, C. R. Williams, W. L. Ecklund, and K. S. Gage, 1998: The effect of vertical air motions on rain rates and median volume diameter determined from combined UHF and VHF wind profiler measurements and comparisons with rain gauge measurements. *J. Atmos. Oceanic Technol.,* **15,** 1306–1319.

——, S. K. Avery, P. T. May, and R. C. Cifelli, 1999: Comparison of precipitation estimation using single- and dual-frequency wind profilers: Simulations and experimental results. *J. Atmos. Oceanic Technol.,* **16,** 165–173.

Rogers, R. R., and R. J. Pilié, 1962: Radar measurements of drop-size distribution. *J. Atmos. Sci.,* **19,** 503–506.

——, D. Baumgardner, S. A. Ethier, D. A. Carter, and W. L. Ecklund, 1993: Comparison of raindrop size distributions measured by radar wind profiler and by airplane. *J. Appl. Meteor.,* **32,** 694–699.

Sato, T., H. Doji, H. Iwai, I. Kimura, S. Fukao, M. Yamamoto, T. Tsuda, and S. Kato, 1990: Computer processing for deriving drop-size distributions and vertical air velocities from VHF Doppler radar spectra. *Radio Sci.,* **25,** 961–973.

Sangren, K. L., P. S. Ray, and G. B. Walker, 1984: A comparison of techniques to estimate vertical air motions and raindrop size distributions. *J. Atmos. Oceanic Technol.,* **1,** 152–165.

Sasyō, Y., and T. Matsuo, 1985: Effects of the variation of falling velocities of snowflakes on their aggregation. *J. Meteor. Soc. Japan,* **63,** 249–261.

Sekhon, R. S., and R. C. Srivastava, 1970: Snow size spectra and radar reflectivity. *J. Atmos. Sci.,* **27,** 299–307.

Smith, P. L., 1984: Equivalent radar reflectivity factors for snow and ice particles. *J. Climate Appl. Meteor.,* **23,** 1258–1260.

Wakasugi, K., A. Mizutani, M. Matsuo, S. Fukao, and S. Kato, 1986: A direct method for deriving drop-size distribution and vertical air velocities from VHF Doppler radar spectra. *J. Atmos. Oceanic Technol.,* **3,** 623–629.

——, ——, ——, ——, and ——, 1987: Further discussion on deriving drop-size distribution and vertical air velocities directly from VHF doppler radar spectra. *J. Atmos. Oceanic Technol.,* **4,** 170–179.

Williams, C. R., 2002: Simultaneous ambient air motion and raindrop size distributions retrieved from UHF vertical incident profiler observations. *Radio Sci.,* **37,** 1024, doi:10.1029/2000RS002603.